Materials Science & Engineering A 766 (2019) 138358

Contents lists available at ScienceDirect

Materials Science & Engineering A

journal homepage: www.elsevier.com/locate/msea

Fatigue behaviour of a laser beam welded CoCrFeNiMn-type high entropy alloy

Nikolai Kashaev[a,*], Volker Ventzke[a], Nikita Petrov[a], Manfred Horstmann[a], Sergey Zherebtsov[b], Dmitry Shaysultanov[b], Vladimir Sanin[c], Nikita Stepanov[b,**]

[a] Institute of Materials Research, Materials Mechanics, Department of Laser Processing and Structural Assessment, Helmholtz-Zentrum Geesthacht, Max-Planck-Str. 1, 21502, Geesthacht, Germany
[b] Belgorod State University, Pobeda 85, Belgorod, 308015, Russia
[c] Institute of Structural Macrokinetics and Materials Science of Russian Academy of Sciences, Academician Osipyan Str. 8, Chernogolovka, Moscow Region, 142432, Russia

ARTICLE INFO

Keywords:
High entropy alloy
Laser beam welding
Microstructure
Tensile strength
Fatigue

ABSTRACT

Laser beam welding was used to produce butt joints from the CoCrFeNiMn-type high entropy alloy. The alloy in the initial condition had an fcc single-phase coarse-grained structure. Laser welding resulted in the M_7C_3-type carbides precipitation in the fcc matrix. The carbide particles precipitation resulted in a considerable increase in microhardness from 150 HV 0.5 for the as-sintered condition to 205 HV 0.5 in the fusion zone. Laser beam welding had a negligible effect on both static mechanical properties and fatigue behaviour of the alloy. The endurance limit of either type of specimens (i.e. with and without welding seam) was 200 MPa. Fracture of all specimens with the laser beam welded seams occurred in the base material area during both tensile and fatigue testing. Weak effect of welding on static/fatigue behaviour of the alloy can be attributed to the higher hardness of the fusion zone, resulting in strain localization in the base material area. An increase in load resulted in activation of secondary slip systems and formation of deformation twins in fatigue specimens.

1. Introduction

Technical progress is often associated with the development of novel materials with advanced properties. For centuries, metallic alloys were used as the structural materials for various applications. However, conventional alloying strategies do not allow further significant progress, required for the most demanding applications in transportation and energy sectors. Therefore the introduction of high entropy alloys (HEAs; also known as complex concentrated alloys, CCAs) concept has attracted considerable attention [1–4]. HEAs, composed of multiple principal elements, can possess unique properties, not readily available in conventional metallic alloys [1,5,6]. This makes HEAs promising candidates for various applications.

The most well-studied class of HEAs composes alloys based on late transition metals [1,7]. Depending on the exact chemical composition, they can have a variety of structures and properties. However, the alloys with the face centered cubic (fcc) structure have attracted special attention. Typical representative of this type of alloys is the equiatomic CoCrFeMnNi alloy [8–11]. This alloy has an fcc single-phase structure stable at temperatures above ≈900°C [12–15] and possess high ductility and toughness at room and cryogenic temperatures [16–18]. However, strength of the alloy at room temperature is rather low. Recent results show that significant improvement of strength without sacrifice of ductility is possible via precipitation hardening [19–24].

Despite extensive investigations of the composition-structure-properties relationships in the transition metals HEAs, many aspects of their behavior remain unclear. For instance, effective welding technologies are required for practical application of materials. It was already shown that different techniques, including arc welding [25], friction stir welding (FSW) [26–29], laser [28,30] and electron beam [25,31] welding can be successfully utilized to produce sound defect-free joints. Mechanical properties of the obtained joints were also found to be promising; in some cases the weld zone had even higher strength than that of the base material [29,30]. This finding was mostly attributed to the precipitation of strengthening second phase particles due to welding.

Another insufficiently explored aspect of HEAs/CCAs behavior concerns their “less general” mechanical properties. Although this alloys are widely considered as promising structural materials, only static compression tests are performed for many of them and thus even tensile

* Corresponding author.
** Corresponding author.
E-mail addresses: nikolai.kashaev@hzg.de (N. Kashaev), stepanov@bsu.edu.ru, stepanov.nikita@icloud.com (N. Stepanov).

https://doi.org/10.1016/j.msea.2019.138358
Received 2 May 2019; Received in revised form 9 July 2019; Accepted 30 August 2019
Available online 30 August 2019
0921-5093/

data may not be available [1,5,6]. However, usually materials undergo much more complex loading with changes in intensity and directions of the applied stresses. However, information on fatigue properties of HEAs is very limited [32–38]. Analysis of the available publications shows that (i) only a couple of works addressed fatigue behavior of single fcc phase alloys [37,39]; the rest deal with more complex multiphase alloys; (ii) the fatigue process is mostly analyzed from the mechanistic viewpoint, while microstructure evolution and deformation mechanisms are basically not addressed [34], in particular in the case of fcc HEAs [39]. Fatigue properties of welded HEAs have never been reported so far in the literature to the best of our knowledge.

Therefore in present work we report fatigue properties and structure evolution of the laser beam welded CoCrFeMnNi-type high entropy alloy. Laser beam welding (LBW) was used as a flexible, industrially feasible process; successful LBW of similar alloys was described earlier in Refs. [28,30].

2. Experimental methods

2.1. Materials and laser beam welding

The program CoCrFeNiMn alloy was produced using thermite-type self-propagating high-temperature synthesis (SHS). The synthesis of the program alloy was carried out in a centrifugal SHS setup. Powders containing oxides of the target elements and Al as the metal reducer were used for the process. Combustion was carried out in a graphite mold with a diameter of 80 mm. The metallic (target) and oxide (slag) layers after the synthesis were easily mechanically separated into two parts: the target alloy and the oxide layer (Al_2O_3). Further details of the alloy preparation procedure can be found elsewhere [29]. The measured chemical composition of the obtained ingot is shown in Table 1. The concentrations of the metallic elements and silicon were measured by energy dispersive spectrometry (EDS) over area $\approx 1 \times 1\,mm^2$, the concentrations of carbon and sulphur were measured using a LECO gas analyser. Note that C, S, and Si found in the alloy were most probably associated with some impurity of the starting oxide powders, while small amount of Al was used as a metal reducer in the initial powder mixture.

Specimens for the welding measured $40 \times 40 \times 2\,mm^3$ were extracted from the as-sintered ingot. Mechanical polishing was used to obtain clear shiny surfaces on each side of the plates. Laser beam welding of the butt joints was performed using an 8.0 kW continuous wave ytterbium fibre laser with a fibre optic (300 μm core diameter and a 300 mm focal length). Butt joints were welded autogenously in a 3-axis Ixion CNC machine in argon atmosphere. The LBW process was performed using the following process parameters:

- The laser power of 2.5 kW;
- The focus position of 0.0 mm above the specimen surface;
- The welding speed of 5 m/min;

These process parameters were identified using previous experiments in order to achieve welds with full penetration and a more “cylindrical” shape of the weld [30].

2.2. Microstructure characterization and mechanical tests

Microstructures, local chemical composition, micro-texture and phase compositions of the laser beam welded butt joints were investigated using scanning electron microscopy (SEM) (Jeol JSM-6490LV) equipped with a back-scattered electron (BSE), an EDS, and an electron back-scatter diffraction (EBSD) (EDAX TSL OIM) detectors. EBSD measurements were performed at 30 kV, an emission current of 75 μA, a sample tilt angle of 70°, a working distance of 14 mm, a magnification of 750 × and a step size of 0.5 μm. The orientation calculation was based on the GSHE method, where triclinic sample symmetry was assumed.

Table 1
Measured chemical composition of the program alloy (in at.-%).

Co	Cr	Fe	Ni	Mn	Al	C	Si	S
19.1	20.0	20.2	19.6	19.2	0.6	0.9	0.3	0.1

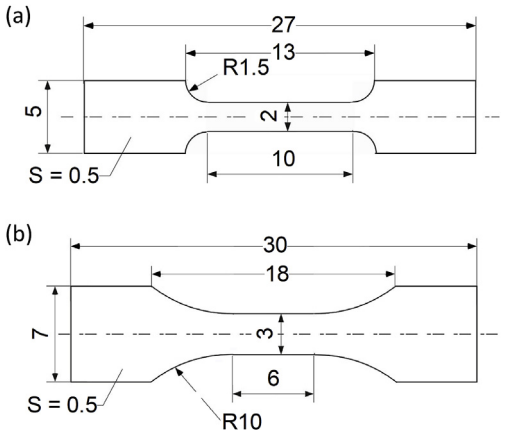

Fig. 1. Geometry of the micro-specimens used in (a) tensile tests and (b) fatigue tests (all of the dimensions are in mm).

The samples for TEM analysis were prepared by conventional twin-jet electro-polishing of mechanically pre-thinned to 100 μm foils, in a mixture of 95% C_2H_5OH and 5% $HClO_4$ at a potential of 27 V. TEM investigations were performed using a JEOL JEM-2100 microscope with an accelerating voltage of 200 kV equipped with an EDS detector.

Microhardness profiles across the joint were obtained using an automated Vickers hardness testing machine with a 0.5 kg load. Micro flat tensile specimens with a thickness of 0.5 mm were extracted via electro discharge machining (EDM) from the as-sintered and welded specimens (Fig. 1). Tensile tests were carried out on a 5-kN electro-mechanic universal testing machine with a constant crosshead speed. The crosshead displacement was measured with a laser extensometer. In the case of fatigue tests a 5-kN high-frequency resonance testing machine was used. The force control fatigue tests were conducted using a sinusoidal wave-form load with a frequency between 123 Hz and 132 Hz. The stress ratio (R) was equal to 0.1 in all tests. The maximal stress of an undamaged fatigue-tested specimen after the number of load cycles $N \geq 10^7$ was identified as the endurance strength at high-cycle fatigue. To obtain stress - load cycles number (S-N) curves, only specimens with a damage within the gauge length were used.

A Thermo-Calc (v. 2017a) software with a specifically developed for HEAs TCHEA2 database was used for the phase diagram construction. However, the TCHEA2 database does not include sulphur, which was found in the alloy (Table 1). Extra amount of Co was added to compensate the absence of S during the calculations.

3. Results and discussion

3.1. Microstructure

Fig. 2a shows a cross-section of the laser beam welded butt joint. The boundary between the joint coupons as well as the boundary between the fusion zone (FZ) and the base metal (BM) is clearly seen. The weld seam width was ~570 μm. Welding defects such as pores or cracks were not identified. Fig. 2b-c illustrates microstructure of the program alloy in the initial (as-sintered) condition and in the fusion zone (FZ) of the weld. The structure of the as-sintered alloy consisted of coarse, elongated, irregularly shaped grains (Fig. 2b). The size of the grains was in the range of 250–500 μm. This type of the as-cast microstructure in

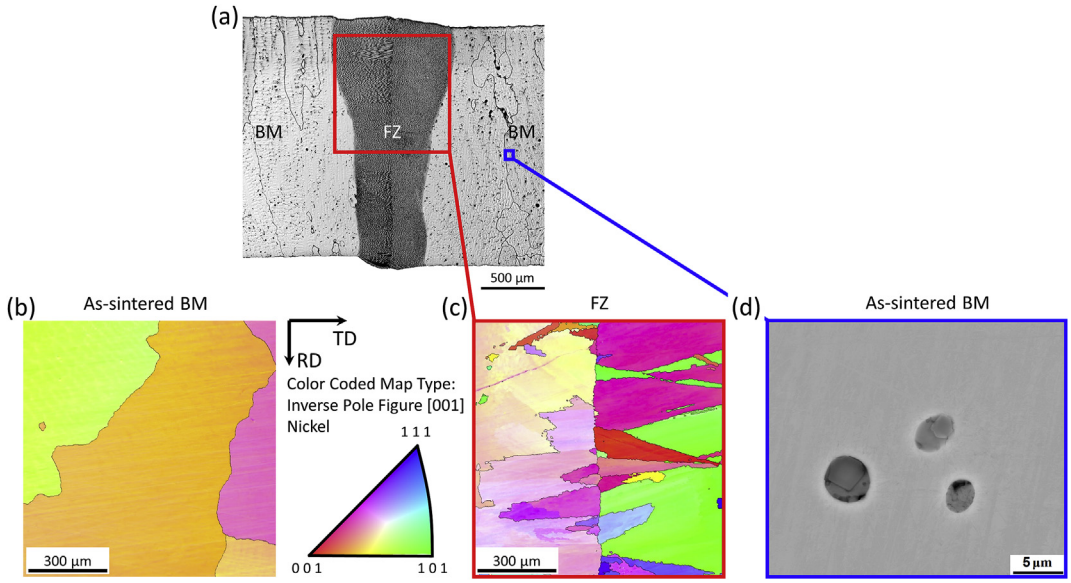

Fig. 2. (a) Micrograph of a LBW butt joint and EBSD IPF maps of the program alloy obtained for the (b) as-sintered material and (c) FZ of the weld. (d) SEM-BSE image of as-sintered BM illustrating MnS inclusions.

the CoCrFeMnNi alloy was reported in a few earlier publications [10,40]. The presence of coarse (~3–5 µm) inclusions, identified as manganese sulfides (MnS) according to some earlier results [30,41], should be noted (Fig. 2d). The MnS inclusions were found both in BM and FZ. Welding resulted in grain refinement to 100–300 µm (Fig. 2c) and the formation of some elongated grains originated from the solidification front. The observed microstructure after welding is also similar to that reported in previous publication [30].

Additional studies were performed using TEM method (Fig. 3). The as-sintered material (Fig. 3a) had an fcc single-phase structure without any signs of second phase(s) precipitations. The microstructure consisted of a number of individual dislocations. LBW resulted in the formation of some second phase particles in the microstructure (Fig. 3b). The particles were found to be enriched with Cr and using selected area electron diffraction patterns they were identified as M_7C_3 type carbides. The size and fraction of the carbides were ~100–200 nm and ~3%, respectively. Some dislocation pileups were found around the carbides. The dislocation density in the laser beam welded material was somewhat higher than in the as-sintered alloy. This finding can be associated with the pinning effect of carbides and with high internal stresses due to rapid cooling of the material after LBW.

A phase diagram of the alloy was constructed to get better understanding of the phase transformations (Fig. 4). Note that MnS inclusions cannot be predicted by Thermo-Calc due to the absence of S in the TCHEA2 database. The alloy solidifies through a single fcc phase field; the liquidus and solidus temperatures are 1315 °C and 1235 °C, respectively. With a decrease in temperature, Cr-rich M_7C_3-type carbides

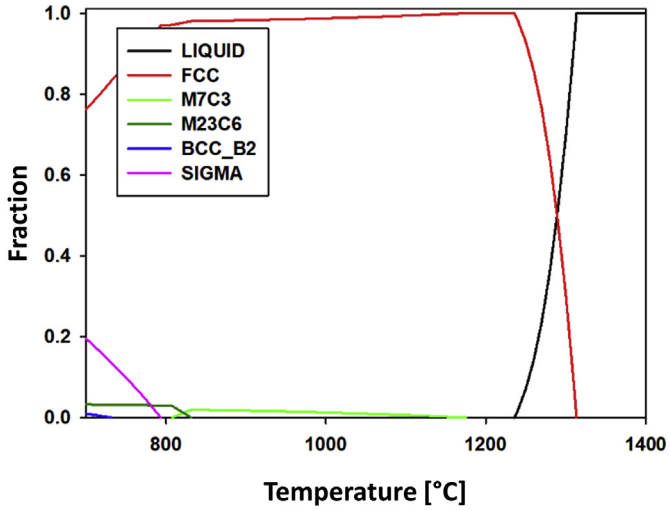

Fig. 4. Phase diagram of the program alloy constructed using the Thermo-Calc software.

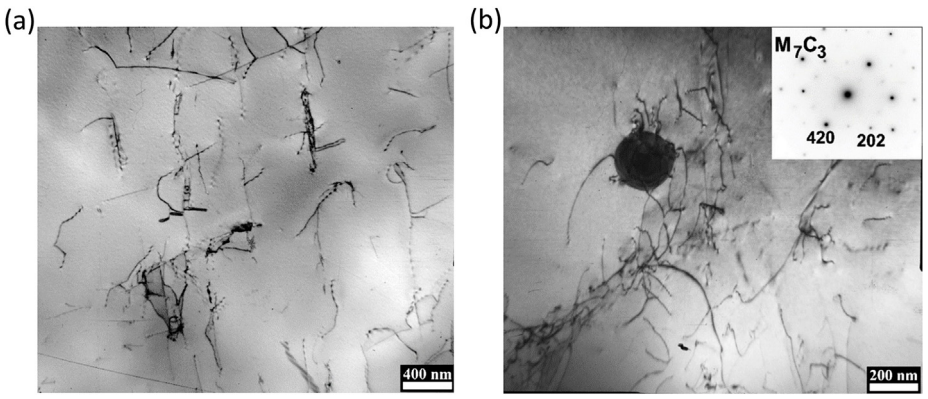

Fig. 3. TEM bright-field image of the structure of the program alloy obtained for (a) the as-sintered and (b) laser beam welded conditions.

appear; the solvus temperature is 1175°C. The carbides fraction slowly increases with a decrease in temperature, and at 805-830°C M_7C_3 transforms into $M_{23}C_6$ carbides. Finally, at even lower temperatures additional phases appear: a Fe, Cr-rich sigma phase and a Ni, Al-rich B2 phase with the solvus temperatures of ≈795°C and ≈730°C, respectively.

The fcc based structure of the examined alloy with a limited amount of inclusions/precipitates (Figs. 2 and 3) was in a reasonable agreement with the calculated phase diagram (Fig. 4). The obtained results demonstrate that laser welding had quite limited effect on structure of the fcc matrix phase, although some changes in grain size and dislocation density occurred (Figs. 2 and 3). The most significant effect of welding was associated with the M_7C_3 carbides precipitation. Precipitation of the nanoscale B2 (NiAl) phase particles during cooling of a laser melted material was earlier reported for an Al-contained CoCrFeMnNi-type alloy [30]. The difference can be associated with variations in the chemical composition of the alloys. The content of Al in the present alloy was noticeably lower than that in the previous report (5.3 at.% vs. 0.6 at.%, respectively); as a result the solvus temperature of the B2 phase was only ≈730°C in comparison with ≈1075 °C in Ref. [30]. Most likely, due to the low solvus temperature the B2 phase particles were not observed in the examined alloy after LBW.

Similarly the solvus temperature of the carbides in the examined alloy (1175 °C) was also somewhat lower than that in the previous work [30] (1225 °C); due to diffusion retardation at temperatures above their solvus the carbides were not found in the as-sintered state. Meanwhile solidification after LBW occurred in somewhat different conditions. It appears that due to different melting temperature and cooling rate diffusion terminated at lower temperature in comparison with that after the SHS process. This suggestion is proved by the results of the previous work, where the B2 phase with the solvus temperature of ≈1075 °C was absent in the as-sintered alloy but appeared after LBW [30].

Precipitation of other type of carbides ($M_{23}C_6$) in the investigated alloy occurred after cold rolling and annealing at 900°C [29]. According to available phase diagram (Fig. 4), the $M_7C_3 \rightarrow M_{23}C_6$ transformation was expected to occur at 805-830°C. The temperature interval of the phase transformation was reasonably close to the annealing temperature used in Ref. [29]. The high-temperature carbides M_7C_3 survival in our case can most likely be associated with relatively fast cooling of the melted material after LBW.

3.2. Microhardness and tensile strength

Microhardness profiles (Fig. 5) were determined across the weld in three regions of the cross-section: the radiation exposure side, middle of the weld and weld root side. The microhardness profiles show a strong increase in microhardness from 150 HV 0.5 for the base material (BM) to 205 HV 0.5 in the fusion zone (FZ). Most likely, the increase in microhardness is associated with the M_7C_3 carbides precipitation (Fig. 3b). Precipitation hardening was recently observed in laser beam welded seams of the similar alloy [30] and was also discussed in terms of structure-properties relationships for carbon-doped HEAs [22,23,42,43]. Grain refinement in the FZ (Fig. 2c) can also contribute to the observed hardening, although its effect was quite modest because of still rather large grain size > 100 μm.

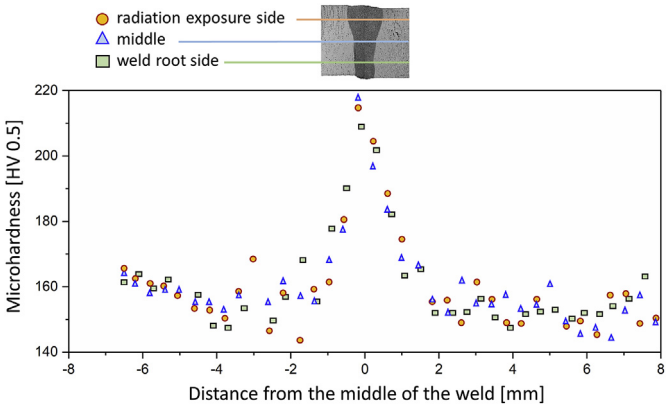

Fig. 5. Microhardness profiles of a laser beam welded butt joint.

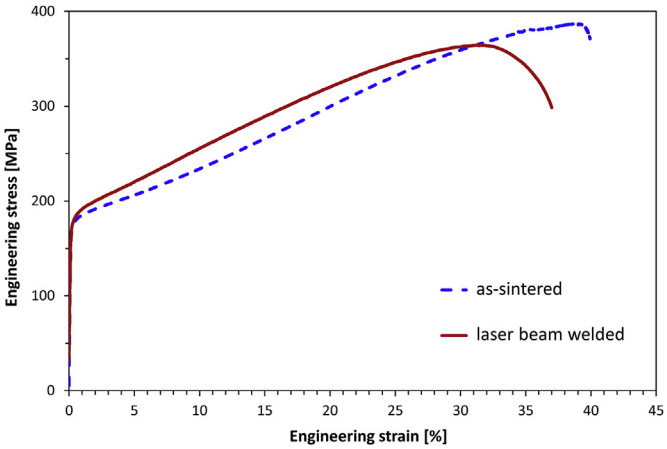

Fig. 6. Engineering stress-strain curves of the program alloy obtained during tensile tests of the as-sintered and laser beam welded specimens. One representative curve for each condition is shown.

Fig. 6 shows static stress-strain curves obtained during tensile tests of the program material with and without laser beam weld. The characteristics such as the yield strength (YS), ultimate tensile strength (UTS), and elongation to fracture (EF) are summarized in Table 2. One can see that welding did not change the mechanical properties substantially. For instance, the yield strength of the as-sintered material was 159 ± 12 MPa, while the laser beam welded specimen yielded at 164 ± 16 MPa. Examination of the tested samples has revealed that the welded specimens always fractured in the BM parts of the gauge aside the FZ. This finding indicates a good quality of the obtained welds and higher hardness (strength) of the FZ (Fig. 5).

The ultimate tensile strength of the alloy in different conditions was also rather close: 362 ± 35 MPa and 349 ± 38 MPa for the as-sintered and laser beam welded conditions, respectively. Due to the higher strength of the laser beam welds, as indicated by the microhardness measurements (Fig. 5), the main deformation of the welded specimens occurred in the BM. As the fracture strain was determined over the whole gauge length and includes the non-plastically deformed weld region, the welded specimens show a slightly reduced value of the elongation to fracture (36.7 ± 0.2%) compared to the values of elongation to fracture for as-sintered material (38.7 ± 0.4%). Similar strength values of the base and welded material were earlier observed in the same alloy after FSW due to hardening of the weld zone and localization of plastic deformation in the base material [29], yet a pronounced decrease in ductility was observed along with nearly identical strength. Some differences in mechanical behaviour of the alloy welded using different techniques can mostly be ascribed to different widths of the welding affected zones: ~0.5 mm after LBW (Fig. 2a) and > 1 mm after FSW [29].

Table 2
Static mechanical properties of the program alloy in the as-sintered and laser beam welded conditions. The average values with standard deviation of three tested specimens are given.

Condition	YS, MPa	UTS, MPa	EF, %
As-sintered	159 ± 12	362 ± 35	38.7 ± 0.4
Laser beam welded	164 ± 16	349 ± 38	36.7 ± 0.2

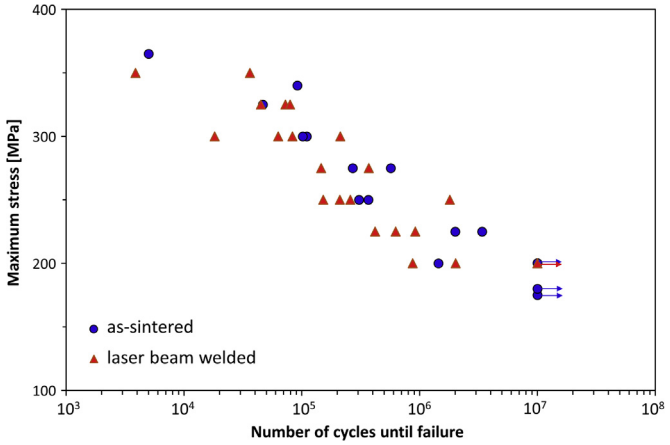

Fig. 7. Fatigue test results. Blue circles and red triangles denote results for the as-sintered and laser beam welded conditions, respectively. (For interpretation of the references to colour in this figure legend, the reader is referred to the Web version of this article.)

3.3. Fatigue behaviour

Numbers of cycles until fracture as a function of maximum applied stress (S-N curve) are shown in Fig. 7. The number of cycles to failure naturally increased with a decrease in the maximum stress. The scatter of experimental points is rather low; in addition, there is no significant difference between the as-sintered and laser beam welded conditions. The endurance limit (the maximum stress for those specimens which reached 10^7 cycles without failure) was determined as 200 MPa for the both conditions. It means that the cyclic stress level for all of the tested specimens was above the material yield strength (~160 MPa, Table 2) and therefore the fracture mechanism during the fatigue test was superimposed with plastic deformation. The ratio between the endurance limit and the tensile strength of the alloy (Table 2) was of ~0.55–0.57. Note that almost the same endurance limit (190 MPa) was recently reported for the CoCrFeNiMn alloy with the grain size of 30 µm [39]. A similar fatigue limit value of the alloy with distinctively different grain sizes (in our case - 250–500 µm (Fig. 2b)) suggests a weak sensitivity of the fatigue behaviour of the alloy to a grain size, at least in the coarse-grained regime.

Similarity of the obtained fatigue properties between as-sintered and laser beam welded conditions is additional indicative of a good quality of the obtained joints. Conventionally, welded joints are considered as "weak" areas of the structures. The present results demonstrate that the laser beam welded CoCrFeMnNi alloy has comparable strength with that of the as-sintered condition both under static (Fig. 6) and cyclic (Fig. 7) loading. This finding can be mostly ascribed to the formation of the "hard" fusion zone (Fig. 5). Therefore plastic flow was mostly localized in those areas which were not affected by laser welding; as such no difference between the as-sintered and laser beam welded material in terms of mechanical properties can be observed. This is an apparent positive ability of the alloy to "intrinsic" hardening during welding due to carbides precipitation [30,44]. However, this effect is important in the case of relatively "weak" BM, with coarse-grained single-phase structure (Figs. 2b and 3a). Presumably, if the base material has higher strength due to a structure with small grains and/or fine precipitates, laser beam welding can result in loss of the strength due to coarsening of grains/precipitates. Nevertheless, a broad HEAs composition range and a flexibility of their microstructure and properties [1,5,45] open ample possibilities to tailor chemical compositions and processing conditions to obtain laser beam welds with high-strength, as it was demonstrated in this work.

3.4. Fracture surfaces

Due to higher strength of the weld (Fig. 5), the fatigue specimens were always fractured in the BM area. Fatigue fracture surfaces of both types (as sintered and laser beam welded) of specimens had three

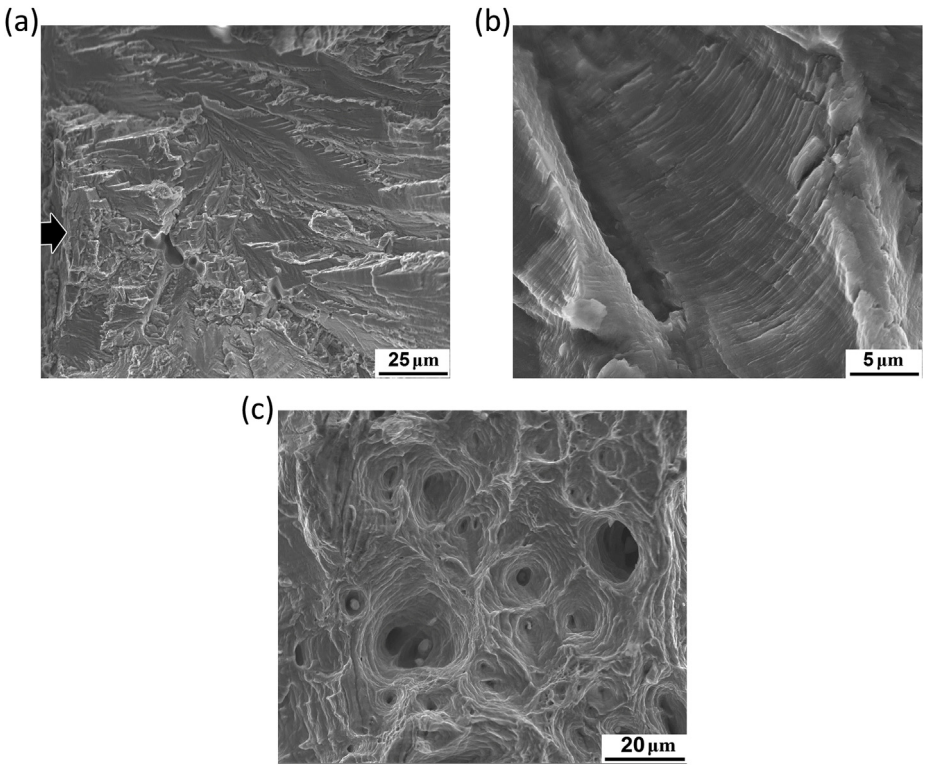

Fig. 8. Fracture surfaces after fatigue test (σ_{max} = 300 MPa, N = 83114 cycles) of the program alloy in the laser beam welded condition: (a) – crack initiation region; (b) – crack propagation region; (c) - overload fracture.

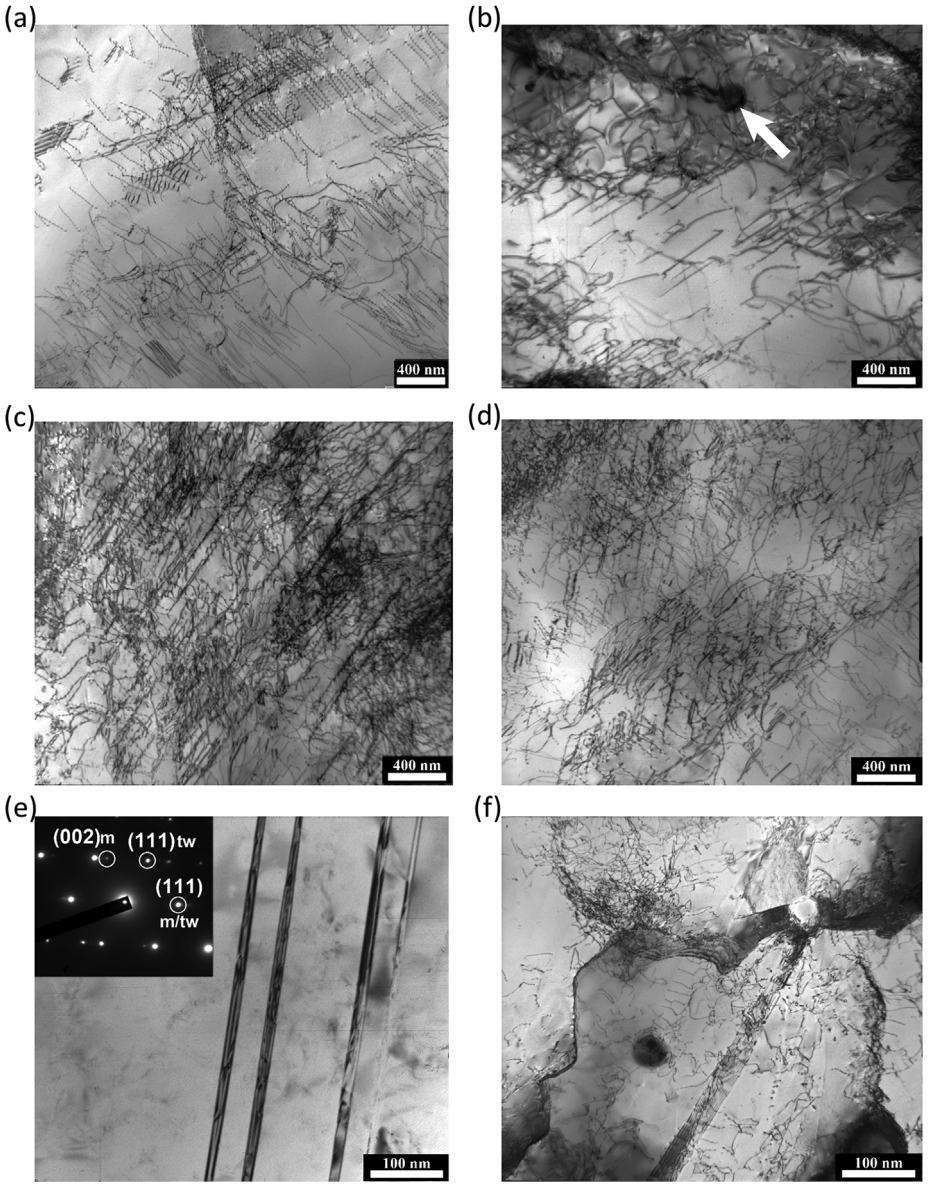

Fig. 9. TEM bright-field images of the program alloy structure in different conditions (as-sintered (a, c, e) and laser beam welded (b, d, f)) after fatigue testing at the maximum stress (σ_{max}) of: (a, b) 200 MPa (not fractured, $N > 10^7$); (c, d) 250 MPa (fractured); (e) 365 MPa (fractured); (f) 350 MPa (fractured). Number of cycles to fracture was equal to: (c) N = 386087; (d) N = 210367; (e) N = 5012; (f) N = 3875.

typical areas: crack initiation, stable fatigue crack propagation and overload fracture. In all cases the fracture started from the specimens' surface. Since the crack tends to follow crystallographic planes during the stage of crack initiation, fatigue fracture surfaces in both cases contained cleavage facet with a feather-like patterns and did not exhibit fatigue striations (Fig. 8a; crack initiation is indicated by an arrow). At the crack propagation stage the fracture surfaces contained clearly recognized fatigue striations. In some cases, the formation of fatigue striations was associated with secondary cracking (Fig. 8b). The final fracture of both types of specimens (as-sintered or laser-beam welded) showed dimpled overload fracture features (Fig. 8c). The nucleation of some dimples was most likely associated with the presence of spherical MnS particles in the microstructure (Fig. 2d). These dimples are usually larger and deeper than the neighbour dimples which do not contain particles at the bottom (Fig. 8c). Carbide particles were not detected at the fracture surfaces; therefore, the effect of carbides on crack initiation during fatigue tests can be considered negligible.

3.5. Microstructure after fatigue tests

To gain better insight into the fatigue behaviour of the alloy, microstructure of the specimens in both conditions (as-sintered and laser beam welded) tested under different maximum cyclic stress was examined using TEM. The obtained images are shown in Fig. 9. After testing at low stresses of 200 MPa (Fig. 9a and b), which did not result in fracture of the specimens, the most pronounced changes were associated with an increase in dislocation density both in as-sintered and laser beam welded conditions (compare with Fig. 3a and b, respectively). Dislocations were mostly formed planar arrays in slip planes. In the laser beam welded condition, some dislocation pileups around carbide particles were found (indicated with arrow in Fig. 9b).

An increase in the maximum stress to 250 MPa increased further dislocation density (Fig. 9c and d). The dislocation motion remained mostly planar, however multiple slip due to the activation of other slip systems can also be observed. The difference in dislocation microstructures between the as-sintered and laser beam welded conditions was negligible. Further increase in stress to 350–365 MPa resulted in

the mechanical twins formation (Fig. 9e) in both conditions of the alloy. The twins had a thickness of 20–30 nm. In some cases a high amount of dislocations partially arranged in cells were observed nearby the twins (Fig. 9f). Although TEM investigations have not provided enough statistics to make a solid statement, it seems that in both conditions the contribution of twinning to stain is noticeably lower than that of dislocation movement.

Although very limited information is available on microstructural response of the CoCrFeMnNi alloy to fatigue deformation [39], microstructure evolution of the alloy during static tensile tests is well documented [16,18]. The investigated alloy, despite some variations in chemistry, shows qualitatively similar behavior: with an increase in testing stress, dislocations gradually evolves from planar dislocation arrays to multiple slip with the further formation of dislocation cells. Some deformation twins were also observed at high testing stresses, yet their fraction was limited. The difference can be found in the relation between the applied stress and the observed deformation mechanism. For instance, during static tension deformation twinning was initiated at a stress of 720 ± 30 MPa [18], while during cyclic experiments twins were already observed at 350–365 MPa. Most probably, this effect is associated with gradual accumulation of dislocations during cyclic deformation.

To sum up the obtained results it should be emphasized that the fatigue tests did not reveal significant differences between the BM specimens and laser beam welded butt joints. Due to higher strength of the weld, the failure occurs in the BM and any possible stress concentrators in the weld as well at the FZ/heat-affected zone or heat-affected zone/BM boundaries do not play any significant role. In addition, high ductility of the program alloy reduces any negative effect of possible stress concentrations through plastic deformation. This allow considering the CoCrFeNiMn-type HEA as promising structural material, which can be joined by means of LBW and then undergo fatigue loading.

4. Conclusions

1) Sound butt joints of the CoCrFeMnNi high entropy alloy were produced using laser beam welding (LBW). In the initial condition, the alloy had an fcc single-phase coarse-grained structure. M_7C_3 type carbides precipitated in the matrix after LBW resulted in a significant hardening of the alloy from 150 HV0.5 for the base material to 205 HV 0.5 in the fusion zone.
2) Tensile properties of the as-sintered and laser beam welded specimens were almost identical; for the both conditions the yield strength and ultimate tensile strength were 159–164 MPa and 349–362 MPa, respectively. Ductility of the welded material was slightly lower than that of the as-sintered alloy: 36.7% and 38.7%, respectively. Welded specimens fractured far from the welding zone due to higher hardness of the seam.
3) Fatigue tests did not reveal significant differences between the as-sintered and laser beam welded material. The endurance limit was 200 MPa for both conditions which corresponded to ~0.55–0.57 of the ultimate tensile strength of the alloy. Fracture of the welded specimens occurred aside the fusion zone.
4) Microstructural examination of the fatigue specimens showed activation of secondary slip systems with an increase in testing stress to 350–365 MPa while only single slip operated at the maximum stress of 250 MPa. Some deformation twins were also observed after testing at the higher stresses. Microstructural response of the alloy during cyclic loading was qualitatively similar to that observed at static tensile tests.

Acknowledgements

The authors would like to thank Mr. R. Dinse, Mr. P. Haack and Mr. F. Dorn from Helmholtz-Zentrum Geesthacht for their valuable technical support. This study was supported by Russian Science Foundation (Grant №18-79-00162).

Appendix A. Supplementary data

Supplementary data to this article can be found online at https://doi.org/10.1016/j.msea.2019.138358.

References

[1] D.B. Miracle, O.N. Senkov, A critical review of high entropy alloys and related concepts, Acta Mater. 122 (2017) 448–511, https://doi.org/10.1016/j.actamat.2016.08.081.
[2] J.-W. Yeh, S.-K. Chen, S.-J. Lin, J.-Y. Gan, T.-S. Chin, T.-T. Shun, C.-H. Tsau, S.-Y. Chang, Nanostructured high-entropy alloys with multiple principal elements: novel alloy design concepts and outcomes, Adv. Eng. Mater. 6 (2004) 299–303, https://doi.org/10.1002/adem.200300567.
[3] E.J. Pickering, N.G. Jones, High-entropy alloys: a critical assessment of their founding principles and future prospects, Int. Mater. Rev. 61 (3) (2016) 183–202, https://doi.org/10.1080/09506608.2016.1180020.
[4] M.-H. Tsai, J.-W. Yeh, High-entropy alloys: a critical review, Mater. Res. Lett. 2 (2014) 107–123, https://doi.org/10.1080/21663831.2014.912690.
[5] S. Gorsse, D.B. Miracle, O.N. Senkov, Mapping the world of complex concentrated alloys, Acta Mater. 135 (2017) 177–187, https://doi.org/10.1016/j.actamat.2017.06.027.
[6] O.N. Senkov, D.B. Miracle, K.J. Chaput, J.-P. Couzinie, Development and exploration of refractory high entropy alloys—a review, J. Mater. Res. 33 (2018) 3092–3128, https://doi.org/10.1557/jmr.2018.153.
[7] Y. Zhang, T.T. Zuo, Z. Tang, M.C. Gao, K.A. Dahmen, P.K. Liaw, Z.P. Lu, Microstructures and properties of high-entropy alloys, Prog. Mater. Sci. 61 (2014), https://doi.org/10.1016/j.pmatsci.2013.10.001.
[8] B. Cantor, I.T.H. Chang, P. Knight, A.J.B. Vincent, Microstructural development in equiatomic multicomponent alloys, Mater. Sci. Eng. A 375 (2004) 213–218, https://doi.org/10.1016/j.msea.2003.10.257.
[9] F. Otto, Y. Yang, H. Bei, E.P.P. George, Relative effects of enthalpy and entropy on the phase stability of equiatomic high-entropy alloys, Acta Mater. 61 (2013) 2628–2638, https://doi.org/10.1016/j.actamat.2013.01.042.
[10] G.A. Salishchev, M.A. Tikhonovsky, D.G. Shaysultanov, N.D. Stepanov, A.V. Kuznetsov, I.V. Kolodiy, A.S. Tortika, O.N. Senkov, Effect of Mn and V on structure and mechanical properties of high-entropy alloys based on CoCrFeNi system, J. Alloy. Comp. 591 (2014) 11–21, https://doi.org/10.1016/j.jallcom.2013.12.210.
[11] M. Laurent-Brocq, A. Akhatova, L. Perrière, S. Chebini, X. Sauvage, E. Leroy, Y. Champion, Insights into the phase diagram of the CrMnFeCoNi high entropy alloy, Acta Mater. 88 (2015), https://doi.org/10.1016/j.actamat.2015.01.068.
[12] B. Schuh, F. Mendez-Martin, B. Völker, E.P. George, H. Clemens, R. Pippan, A. Hohenwarter, Mechanical properties, microstructure and thermal stability of a nanocrystalline CoCrFeMnNi high-entropy alloy after severe plastic deformation, Acta Mater. 96 (2015) 258–268, https://doi.org/10.1016/j.actamat.2015.06.025.
[13] E.J. Pickering, R. Muñoz-Moreno, H.J. Stone, N.G. Jones, Precipitation in the equiatomic high-entropy alloy CrMnFeCoNi, Scr. Mater. 113 (2016) 106–109, https://doi.org/10.1016/j.scriptamat.2015.10.025.
[14] F. Otto, A. Dlouhý, K.G. Pradeep, M. Kuběnová, D. Raabe, G. Eggeler, E.P. George, Decomposition of the single-phase high-entropy alloy CrMnFeCoNi after prolonged anneals at intermediate temperatures, Acta Mater. 112 (2016) 40–52, https://doi.org/10.1016/j.actamat.2016.04.005.
[15] M.V. Klimova, D.G. Shaysultanov, S.V. Zherebtsov, N.D. Stepanov, Effect of second phase particles on mechanical properties and grain growth in a CoCrFeMnNi high entropy alloy, Mater. Sci. Eng. A 748 (2019) 228–235, https://doi.org/10.1016/J.MSEA.2019.01.112.
[16] F. Otto, A. Dlouhý, C. Somsen, H. Bei, G. Eggeler, E.P. George, The influences of temperature and microstructure on the tensile properties of a CoCrFeMnNi high-entropy alloy, Acta Mater. 61 (2013) 5743–5755, https://doi.org/10.1016/j.actamat.2013.06.018.
[17] B. Gludovatz, A. Hohenwarter, D. Catoor, E.H. Chang, E.P. George, R.O. Ritchie, A fracture-resistant high-entropy alloy for cryogenic applications, Science 345 (6201) (2014) 1153–1158, https://doi.org/10.1126/science.1254581.
[18] G. Laplanche, A. Kostka, O.M.M. Horst, G. Eggeler, E.P.P. George, Microstructure evolution and critical stress for twinning in the CrMnFeCoNi high-entropy alloy, Acta Mater. 118 (2016) 152–163, https://doi.org/10.1016/j.actamat.2016.07.038.
[19] T. Yang, Y.L. Zhao, J.H. Luan, B. Han, J. Wei, J.J. Kai, C.T. Liu, Nanoparticles-strengthened high-entropy alloys for cryogenic applications showing an exceptional strength-ductility synergy, Scr. Mater. 164 (2019) 30–35, https://doi.org/10.1016/J.SCRIPTAMAT.2019.01.034.
[20] Y. Tong, D. Chen, B. Han, J. Wang, R. Feng, T. Yang, C. Zhao, Y.L. Zhao, W. Guo, Y. Shimizu, C.T. Liu, P.K. Liaw, K. Inoue, Y. Nagai, A. Hu, J.J. Kai, Outstanding tensile properties of a precipitation-strengthened FeCoNiCrTi0.2 high-entropy alloy at room and cryogenic temperatures, Acta Mater. 165 (2019) 228–240, https://doi.org/10.1016/J.ACTAMAT.2018.11.049.
[21] J.Y. He, H. Wang, H.L. Huang, X.D. Xu, M.W. Chen, Y. Wu, X.J. Liu, T.G. Nieh, K. An, Z.P. Lu, A precipitation-hardened high-entropy alloy with outstanding tensile properties, Acta Mater. 102 (2016) 187–196, https://doi.org/10.1016/j.actamat.2015.08.076.

[22] M.V. Klimova, D.G. Shaysultanov, R.S. Chernichenko, V.N. Sanin, N.D. Stepanov, S.V. Zherebtsov, A.N. Belyakov, Recrystallized microstructures and mechanical properties of a C-containing CoCrFeNiMn-type high-entropy alloy, Mater. Sci. Eng. A (2019) 740–741, https://doi.org/10.1016/J.MSEA.2018.09.113 201–210.
[23] N.D. Stepanov, N.Y. Yurchenko, M.A. Tikhonovsky, G.A. Salishchev, Effect of carbon content and annealing on structure and hardness of the CoCrFeNiMn-based high entropy alloys, J. Alloy. Comp. 687 (2016) 59–71, https://doi.org/10.1016/j.jallcom.2016.06.103.
[24] B. Gwalani, S. Gorsse, D. Choudhuri, M. Styles, Y. Zheng, R.S. Mishra, R. Banerjee, Modifying transformation pathways in high entropy alloys or complex concentrated alloys via thermo-mechanical processing, Acta Mater. 153 (2018) 169–185, https://doi.org/10.1016/J.ACTAMAT.2018.05.009.
[25] Z. Wu, S.A. David, D.N. Leonard, Z. Feng, H. Bei, Microstructures and mechanical properties of a welded CoCrFeMnNi high-entropy alloy, Sci. Technol. Weld. Join. 23 (7) (2018) 585–595, https://doi.org/10.1080/13621718.2018.1430114.
[26] Z.G. Zhu, Y.F. Sun, F.L. Ng, M.H. Goh, P.K. Liaw, H. Fujii, Q.B. Nguyen, Y. Xu, C.H. Shek, S.M.L. Nai, J. Wei, Friction-stir welding of a ductile high entropy alloy: microstructural evolution and weld strength, Mater. Sci. Eng. A 711 (2018) 524–532, https://doi.org/10.1016/J.MSEA.2017.11.058.
[27] Z.G. Zhu, Y.F. Sun, M.H. Goh, F.L. Ng, Q.B. Nguyen, H. Fujii, S.M.L. Nai, J. Wei, C.H. Shek, Friction stir welding of a $CoCrFeNiAl_{0.3}$ high entropy alloy, Mater. Lett. 205 (2017) 142–144, https://doi.org/10.1016/j.matlet.2017.06.073.
[28] M.-G. Jo, H.-J. Kim, M. Kang, P.P. Madakashira, E.S. Park, J.-Y. Suh, D.-I. Kim, S.-T. Hong, H.N. Han, Microstructure and mechanical properties of friction stir welded and laser welded high entropy alloy CrMnFeCoNi, Met. Mater. Int. 24 (2018) 73–83, https://doi.org/10.1007/s12540-017-7248-x.
[29] D. Shaysultanov, N. Stepanov, S. Malopheyev, I. Vysotskiy, V. Sanin, S. Mironov, R. Kaibyshev, G. Salishchev, S. Zherebtsov, Friction stir welding of a carbon-doped CoCrFeNiMn high-entropy alloy, Mater. Char. 145 (2018) 353–361, https://doi.org/10.1016/J.MATCHAR.2018.08.063.
[30] N. Kashaev, V. Ventzke, N. Stepanov, D. Shaysultanov, V. Sanin, S. Zherebtsov, Laser beam welding of a CoCrFeNiMn-type high entropy alloy produced by self-propagating high-temperature synthesis, Intermetallics 96 (2018) 63–71, https://doi.org/10.1016/j.intermet.2018.02.014.
[31] Z. Wu, S.A. David, Z. Feng, H. Bei, Weldability of a high entropy CrMnFeCoNi alloy, Scr. Mater. 124 (2016) 81–85, https://doi.org/10.1016/j.scriptamat.2016.06.046.
[32] M.A. Hemphill, T. Yuan, G.Y. Wang, J.W. Yeh, C.W. Tsai, A. Chuang, P.K. Liaw, Fatigue behavior of Al0.5CoCrCuFeNi high entropy alloys, Acta Mater. 60 (2012) 5723–5734, https://doi.org/10.1016/j.actamat.2012.06.046.
[33] M. Seifi, D. Li, Z. Yong, P.K. Liaw, J.J. Lewandowski, Fracture toughness and fatigue crack growth behavior of as-cast high-entropy alloys, JOM 67 (2015) 2288–2295, https://doi.org/10.1007/s11837-015-1563-9.
[34] Z. Tang, T. Yuan, C.-W. Tsai, J.-W. Yeh, C.D. Lundin, P.K. Liaw, Fatigue behavior of a wrought Al0.5CoCrCuFeNi two-phase high-entropy alloy, Acta Mater. 99 (2015) 247–258, https://doi.org/10.1016/j.actamat.2015.07.004.
[35] K. Liu, M. Komarasamy, B. Gwalani, S. Shukla, R.S. Mishra, Fatigue behavior of ultrafine grained triplex Al0.3CoCrFeNi high entropy alloy, Scr. Mater. 158 (2019) 116–120, https://doi.org/10.1016/J.SCRIPTAMAT.2018.08.048.
[36] P. Chen, C. Lee, S.-Y. Wang, M. Seifi, J.J. Lewandowski, K.A. Dahmen, H. Jia, X. Xie, B. Chen, J.-W. Yeh, C.-W. Tsai, T. Yuan, P.K. Liaw, Fatigue behavior of high-entropy alloys: a review, Sci. China Technol. Sci. 61 (2018) 168–178, https://doi.org/10.1007/s11431-017-9137-4.
[37] K.V.S. Thurston, B. Gludovatz, A. Hohenwarter, G. Laplanche, E.P. George, R.O. Ritchie, Effect of temperature on the fatigue-crack growth behavior of the high-entropy alloy CrMnFeCoNi, Intermetallics 88 (2017) 65–72, https://doi.org/10.1016/J.INTERMET.2017.05.009.
[38] B. Guennec, V. Kentheswaran, L. Perrière, A. Ueno, I. Guillot, J.-P. Couzinié, G. Dirras, Four-point bending fatigue behavior of an equimolar BCC HfNbTaTiZr high-entropy alloy: macroscopic and microscopic viewpoints, Materialia 4 (2018) 348–360, https://doi.org/10.1016/J.MTLA.2018.09.040.
[39] Y.Z. Tian, S.J. Sun, H.R. Lin, Z.F. Zhang, Fatigue behavior of CoCrFeMnNi high-entropy alloy under fully reversed cyclic deformation, J. Mater. Sci. Technol. 35 (2019) 334–340, https://doi.org/10.1016/J.JMST.2018.09.068.
[40] N.D. Stepanov, D.G. Shaysultanov, G.A. Salishchev, M.A. Tikhonovsky, E.E. Oleynik, A.S. Tortika, O.N. Senkov, Effect of V content on microstructure and mechanical properties of the CoCrFeMnNiVx high entropy alloys, J. Alloy. Comp. 628 (2015) 170–185, https://doi.org/10.1016/j.jallcom.2014.12.157.
[41] N. Choi, K.R. Lim, Y.S. Na, U. Glatzel, J.H. Park, Characterization of non-metallic inclusions and their influence on the mechanical properties of a FCC single-phase high-entropy alloy, J. Alloy. Comp. 763 (2018) 546–557, https://doi.org/10.1016/j.jallcom.2018.05.339.
[42] Z. Li, C.C. Tasan, H. Springer, B. Gault, D. Raabe, Interstitial atoms enable joint twinning and transformation induced plasticity in strong and ductile high-entropy alloys, Sci. Rep. 7 (2017) 40704, https://doi.org/10.1038/srep40704.
[43] J.Y. Ko, S.I. Hong, Microstructural evolution and mechanical performance of carbon-containing CoCrFeMnNi-C high entropy alloys, J. Alloy. Comp. 743 (2018) 115–125, https://doi.org/10.1016/j.jallcom.2018.01.348.
[44] P. Kürnsteiner, M.B. Wilms, A. Weisheit, P. Barriobero-Vila, E.A. Jägle, D. Raabe, Massive nanoprecipitation in an Fe-19Ni-xAl maraging steel triggered by the intrinsic heat treatment during laser metal deposition, Acta Mater. 129 (2017) 52–60, https://doi.org/10.1016/j.actamat.2017.02.069.
[45] B. Gwalani, S. Gorsse, D. Choudhuri, Y. Zheng, R.S. Mishra, R. Banerjee, Tensile yield strength of a single bulk Al0.3CoCrFeNi high entropy alloy can be tuned from 160 MPa to 1800 MPa, Scr. Mater. 162 (2019) 18–23, https://doi.org/10.1016/J.SCRIPTAMAT.2018.10.023.